



Efficiency enhancement of Raman spectroscopy at long working distance by parabolic reflector

YAO TIAN,^{1,2} JOSHUA WEIMING SU,^{1,2} JIAN JU,¹ AND QUAN LIU^{1,*}

¹School of Chemical and Biomedical Engineering, Nanyang Technological University, 62 Nanyang Dr. 637459, Singapore

²These two authors contributed equally

*quanliu@ntu.edu.sg

Abstract: Raman spectroscopy is well suited for readily revealing information about bio-samples. As such, this technique has been applied to a wide range of areas, particularly in bio-medical diagnostics. Raman scattering in bio-samples typically has a low signal level due to the nature of inelastic scattering of photons. To achieve a high signal level, usually a high numerical aperture objective is employed. One drawback with these objectives is that their working distance is very short. However, in many cases of clinical diagnostics, a long working distance is preferable. We propose a practical solution to this problem by enhancing the Raman signal using a parabolic reflector. The high signal level is achieved through the large light collection solid angle of the parabolic reflector while the long working distance is ensured by the novel design of our microscope. The enhancement capability of the microscope was demonstrated on four types of samples. Among these samples, we find that this microscope design is most suitable for turbid samples.

© 2017 Optical Society of America

OCIS codes: (180.0180) Microscopy; (170.5660) Raman spectroscopy.

References and links

1. R. L. McCreery, *Raman Spectroscopy for Chemical Analysis*, vol. 225 (John Wiley & Sons, 2005).
2. Y. Tian, M. J. Gray, H. Ji, R. J. Cava, and K. S. Burch, "Magneto-elastic coupling in a potential ferromagnetic 2d atomic crystal," *2D Mater.* **3**(2), 025035 (2016).
3. Y. Tian, G. B. Osterhoudt, S. Jia, R. Cava, and K. S. Burch, "Local phonon mode in thermoelectric Bi₂Te₂Se from charge neutral antisites," *Appl. Phys. Lett.* **108**(4), 041911 (2016).
4. Y. Tian, S. Jia, R. Cava, R. Zhong, J. Schneeloch, G. Gu, and K. S. Burch, "Understanding the evolution of anomalous anharmonicity in Bi₂Te_{3-x}Se_x," *Phys. Rev. B* **95**(9), 094104 (2017).
5. C. Perlaki, S. Lim, and Q. Liu, "Polarized Raman spectroscopy for enhanced quantification of protein concentrations in an aqueous mixture," *J. Raman Spectrosc.* **46**(9), 744–749 (2015).
6. K. Chen, C. Yuen, Y. Aniwah, P. Preiser, and Q. Liu, "Towards ultrasensitive malaria diagnosis using surface enhanced Raman spectroscopy," *Sci. Rep.* **6**, 20177–20186 (2016).
7. C. M. Perlaki, Q. Liu, and M. Lim, "Raman spectroscopy based techniques in tissue engineering—an overview," *Appl. Spectrosc. Rev.* **49**(7), 513–532 (2014).
8. G. McLaughlin, K. C. Doty, and I. K. Lednev, "Raman spectroscopy of blood for species identification," *Anal. Chem.* **86**(23), 11628–11633 (2014).
9. M. Elshout, R. J. Erckens, C. A. Webers, H. J. Beckers, T. T. Berendschot, J. de Brabander, F. Hendrikse, and J. S. Schouten, "Detection of Raman spectra in ocular drugs for potential in vivo application of Raman spectroscopy," *J. Ocul. Pharmacol. Th.* **27**(5), 445–451 (2011).
10. N. J. Bauer, F. Hendrikse, and W. F. March, "In vivo confocal Raman spectroscopy of the human cornea," *Cornea* **18**(4), 483–488 (1999).
11. C. L. Evans, E. O. Potma, M. Puoris' haag, D. Côté, C. P. Lin, and X. S. Xie, "Chemical imaging of tissue in vivo with video-rate coherent anti-stokes Raman scattering microscopy," *Proc. Natl. Acad. Sci. U.S.A.* **102**(46), 16807–16812 (2005).
12. H.-U. Gremlich and B. Yan, *Infrared and Raman Spectroscopy of Biological Materials* (CRC Press, 2000).
13. S. Chen, Y. H. Ong, and Q. Liu, "Fast reconstruction of Raman spectra from narrow-band measurements based on Wiener estimation," *J. Raman Spectrosc.* **44**(6), 875–881 (2013).
14. D. Zhang, X. Wang, K. Braun, H.-J. Egelhaaf, M. Fleischer, L. Hennemann, H. Hintz, C. Stanciu, C. J. Brabec, D. P. Kern *et al.*, "Parabolic mirror-assisted tip-enhanced spectroscopic imaging for non-transparent materials," *J. Raman Spectrosc.* **40**(10), 1371–1376 (2009).
15. A. Yu, D. Zuo, J. Gao, B. Li, and X. Wang, "Application of parabolic reflector on Raman analysis of gas samples," *Proc. SPIE* **9855**, 98550A (2016).

16. A. Ahmed, Y. Pang, G. Hajisalem, and R. Gordon, "Antenna design for directivity-enhanced raman spectroscopy," *Int. J. Opt.* **2012**, 729138 (2012).
17. A. K. Misra, S. K. Sharma, L. Kamemoto, P. V. Zinin, Q. Yu, N. Hu, and L. Melnick, "Novel micro-cavity substrates for improving the raman signal from submicrometer size materials," *Appl. Spectrosc.* **63**(3), 373–377 (2009).
18. G. Turrell and J. Corset, *Raman Microscopy: Developments and Applications* (Academic Press, 1996).
19. K. Tanaka, M. T. Pacheco, J. F. Brennan, I. Itzkan, A. J. Berger, R. R. Dasari, and M. S. Feld, "Compound parabolic concentrator probe for efficient light collection in spectroscopy of biological tissue," *Appl. Opt.* **35**(4), 758–763 (1996).
20. C.-R. Kong, I. Barman, N. C. Dingari, J. W. Kang, L. Galindo, R. R. Dasari, and M. S. Feld, "A novel non-imaging optics based raman spectroscopy device for transdermal blood analyte measurement," *AIP Adv.* **1**(3), 032175 (2011).
21. J. Mathew, Y. Semenova, and G. Farrell, "A miniature optical breathing sensor," *Biomed. Opt. Express* **3**(12), 3325–3331 (2012).
22. C. Yuen and Q. Liu, "Hollow agarose microneedle with silver coating for intradermal surface-enhanced raman measurements: a skin-mimicking phantom study," *J. Biomed. Opt.* **20**(6), 061102 (2015).
23. R. Liu, M. Zhang, and C. Jin, "In vivo and in situ imaging of controlled-release dissolving silk microneedles into the skin by optical coherence tomography," *J. Biophotonics* **10**(6-7), 870–877 (2017).
24. C. A. Lieber and A. Mahadevan-Jansen, "Automated method for subtraction of fluorescence from biological raman spectra," *Appl. Spectrosc.* **57**(11), 1363–1367 (2003).
25. L. G. Coppel, N. Johansson, and M. Neuman, "Angular dependence of fluorescence from turbid media," *Opt. Express* **23**(15), 19552–19564 (2015).
26. C. Mätzler, "Matlab functions for mie scattering and absorption, version 2," *IAP Res. Rep* **8**, 1–24 (2002).
27. J. M. Geary, *Introduction to Lens Design: With Practical ZEMAX Examples* (Willmann-Bell Richmond, 2002).

1. Introduction

Raman spectroscopy is well suited for readily revealing molecular information of samples. As such, this technique has been applied to a wide range of areas including chemistry [1], physics [2–4], and biology [5]. As a label-free and non-destructive technique, Raman spectroscopy has become a promising tool for analyzing bio-samples in clinical diagnostics [6,7]. However, many bio-samples are easily deformable and some are even in solution, making measurements extremely tricky [8]. To avoid contamination, usually a long working distance objective needs to be employed [9–11]. These objective lenses usually have a very steep price curve; as their numerical aperture (NA) increases, their price increases significantly. Due to budget limitations, an objective with lower NA is frequently chosen instead and, since signal collection efficiency is proportional to NA^2 , signal collection efficiency is sacrificed. Moreover, many bio-samples have weak Raman signals [12]. Hence, to obtain reliable data with low NA objectives, one has to prolong the integration time, which is both time consuming and costly. To speed up the acquisition, the wavelength integration method was developed. However, assumptions or prior knowledge are required to reconstruct the original spectra from integrated measurements [13].

In this paper, we propose a microscope design to address these issues that is practical, simple, and less costly. The design involves incorporating a parabolic reflector into a custom-built Raman microscope, significantly improving the signal collection efficiency of the microscope due to the large acceptance angle of the reflector. There have been some studies using parabolic reflectors and other aspherical mirrors for signal collection. Zhang *et al.* used a parabolic reflector in a tip-enhanced Raman microscope to assist measurements of different chemical components in solar cell blend film [14]. Yu *et al.* utilized a parabolic reflector for both excitation and signal collection to improve the sensitivity of gas detection [15]. Ahmed *et al.* enhanced the directivity of Raman emission through the novel design of a parabolic mirror nano-antenna [16]. Misra *et al.* fabricated a micro-cavity and used it to enhance the Raman response of samples trapped inside the cavity [17]. Two half coaxial ellipsoidal mirrors can also be used to increase the signal collection efficiency [18]. These techniques require either transparent/small samples or customized and expensive optics, which is hard to fulfill in many cases. Researchers have also found that non-imaging optics such as compound hyperbolic concentrators and compound parabolic concentrators can significantly enhance Raman signals [19,20]. However, this technique results in a larger illumination spot size and requires complex optics. To the best of our knowledge,

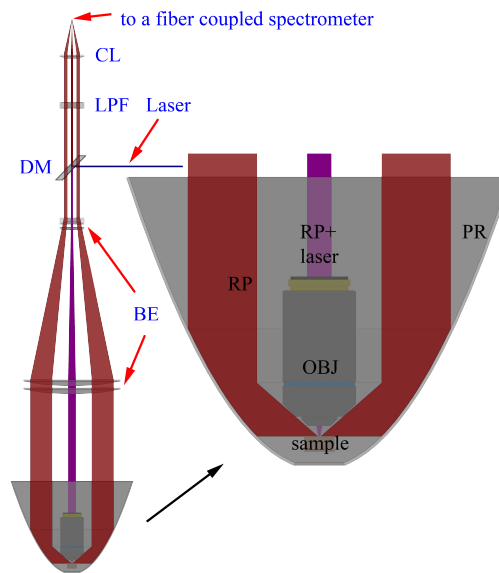


Fig. 1. Schematic of the customized Raman microscope. The laser (represented by the blue ray) from the right side is directed downwards by the dichroic mirror. The Raman photons are represented by the red rays. The optical path shared by the laser and Raman photons is shown in magenta. Abbreviations refer to the following: dichroic mirror (DM), beam expander (BE which consists of four lens, see Appendix 6.2 for the detailed design), long-pass filter (LPF), collection lens (CL), Raman photons (RP), objective lens (OBJ), and parabolic reflector (PR).

there is no study that incorporates a commercially available parabolic reflector into a conventional Raman microscope in which excitation is achieved using an objective lens and the signal collection is aided by a parabolic reflector. We fill this gap with a novel Raman microscope design which features high signal collection efficiency while simultaneously maintaining a long working distance. To demonstrate the capability of our setup, we measured four different types of samples: a hydrotalcite tablet, Rhodamine 6G dissolved in an agarose gel media mixed with surface enhancement agents, a piece of bacon fat, and crystalline silicon. The first three samples are frequently seen in the pharmaceutical industry and biological research; the last one is widely used in the alignment and calibration of Raman systems. We found that, among all the samples, the turbid samples yielded better enhancement results. We attribute this to differences in the angle of emission and additional scattering inside the sample media after the Raman photons are emitted. Our system is relatively simple and all optics are commercially available, which opens the door for enhancing collection efficiency, of a customized Raman system or a simple upgrade to an existing Raman system, with a minimal amount of modification.

2. Operating principles

In this section, we focus on the signal enhancement design principle. Before we delve into the principle, it is worthwhile to walk through the entire setup first. For this purpose, we illustrate the schematics of our microscope in Fig. 1. The laser beam (Thorlabs, Inc., HNL225R-EC, 632.8 nm, shown by the blue ray) is directed down from the side by a dichroic mirror (DM). After the dichroic mirror, the beam path is labelled in magenta since the beam path of the laser is shared with the scattered photons. Next, the laser beam is enlarged by a beam expander (BE) and focused through an inexpensive, long working distance objective (OBJ, CFI-POL 20x, Nikon

Corporation, working distance = 3.9 mm, NA = 0.4) onto a sample. After illumination, a portion of the scattered light (Raman, Rayleigh and fluorescence scattering) is collected by the objective. Simultaneously, a separate portion of the scattered light is reflected upwards by a parabolic reflector (PR, Newport Corporation, PARAB-01, diameter = 101.6mm, $f = 10.2$ mm, clear aperture = 124.5 mm), forming a much larger collimated beam which is shrunk by the beam expander to accommodate the size of the dichroic mirror. To the best of our knowledge, there is no commercially available beam expander capable of shrinking a beam of such a large size (about 90 mm). Hence, we designed a beam expander for this purpose, the details of which are given in Appendix 6.2. Finally, both portions of the scattered light, after passing through the dichroic mirror and a long-pass filter (LPF), are focused by a collection lens (CL, Thorlabs, Inc., $f = 30$ mm, AC254-030-B-ML) into an optical fiber (Thorlabs, Inc., M200L02S-A, $\varnothing = 200\mu\text{m}$, NA=0.22) coupled spectrometer (Princeton Instruments, Acton SP2100, not shown), and recorded by a CCD detector (Princeton Instruments, PIXIS 400, not shown).

Bearing the photon propagation in mind, let us move on to the signal enhancement design principle, which is illustrated by the inset image in Fig. 1. Based on the geometry, we calculated that, for the objective, the angle of collection relative to its optical axis is from 0° to 23.4° . For the PR, the angle of collection is from 36.3° to 90° but photons with an angle of emission between 23.4° to 45° will be blocked by the barrel of the objective. Thus, the effective angle of acceptance of the PR is from 45° to 90° . Consequently, assuming scattered photons are emitted nearly isotropically, the majority of photons can be collected, given the large solid angle of acceptance of the PR, resulting in an enhancement effect. To ensure that these photons are reflected upwards, the alignment between the objective and the PR is critical. For this purpose, the reflector is coupled to a kinematic mount fixed on a tri-axis translation stage, leading to five degrees of freedom (yaw, pitch, x , y and z) to align the reflector. For details about the alignment procedure, please refer to Appendix 6.4. It is worth noting that in the statement above, we chose to ignore those photons emitted downwards (emission angle $> 90^\circ$) and then reflected upwards by the back surface of a sample, since the samples that we used to demonstrate the enhancement effect are all opaque and have mean free paths or penetration depths much shorter than their thicknesses.

3. Experiment results

To demonstrate the enhancement capability of our setup, we performed Raman measurements on four types of samples. These four samples are a hydrotalcite tablet (HT), which is a powder-based tablet, a dosage form commonly used in the pharmaceutical industry; a piece of crystalline silicon which is widely used for calibration of Raman systems; Rhodamine 6G (R6G) dissolved in an agarose gel media mixed with surface enhancement agents and a piece of sliced bacon fat, which are both samples usually seen in biomedical optics research [21–23]. During the measurement, the spectra were taken with the focal point of the PR significantly displaced from the focal point of the objective and the position of the sample was finely tuned to achieve the highest signal level, without the signal from the PR. Following this, the focal point of the PR was aligned with the focal point of the objective and the sample was measured again with identical parameters. For each measurement, 20 acquisitions, with a time of 10 seconds per acquisition, were added up with the laser power set at 10 mW on the sample. To see the enhancement effect for the Raman features, the raw spectra were preprocessed by extracting the fluorescence background using a modified polynomial fit approach [24], and subtracting the fluorescence background from the spectra. Consequently, two spectra (obtained with and without the PR) were generated for each sample, as shown in Fig. 2. Clearly, the enhancement effect was observed in all four samples. To quantify the enhancement factor, we fit the two processed spectra obtained with and without the PR using:

$$R_{PR+OBJ}(\nu) = \alpha \times R_{OBJ}(\nu) \quad (1)$$

where the constant α can be taken as the enhancement factor, ν is the wavenumber, and $R_{PR+OBJ}(\nu)$ and $R_{OBJ}(\nu)$ represent the two spectra obtained with and without the PR. The resulting enhancement factors with its confidence interval are shown in red in the figure. For HT, we found an approximately 5.3 times enhancement of Raman features. The R6G sample was dissolved in agarose gel with Ag nano-particles embedded. The nano-particles here serve as the surface enhancement agent. Details about sample preparation can be found elsewhere [22]. For this sample, the Raman enhancement is about 3.9 times. In the third sample, a piece of sliced bacon fat, a 2.3 times Raman enhancement was observed. We only saw a factor of 1.3 times enhancement in the last sample, silicon. We attribute this effect to the different turbidity of the samples which will be discussed in detail in Sec. 4.

For a performance comparison, we also measured the same samples using a high-NA objective (Olympus, UMPlanFI, NA = 0.8, working distance = 0.66 mm) with the same experiment parameters. We followed the same procedure for spectral processing and the results are presented in Fig. 2. We can see that the enhancement factors obtained by the high-NA objective are more or less constants varying from 3.15 to 4.24. The enhancement factors achieved by the PR are comparable to the high-NA objective for the first two samples and less in the last two samples.

4. Discussion

A variation in the enhancement factors among the four samples was observed. We attribute this effect to differences in the angle of emission and additional scattering inside the sample media after the Raman photons are emitted. Let us consider the case of silicon first. The angle of emission of Raman photons is determined by the momentum of the outgoing photons. Assuming the momentum of the incoming photon is \vec{K}_i and that of the outgoing photon is \vec{K}_o , the momentum \vec{q}_R transferred to the sample therefore equals $\vec{K}_i - \vec{K}_o$. The energy transferred (ω_R) is given by the energy difference between the two photons, denoted by $E_i - E_o$. In crystalline samples, due to the discrete translation symmetry, ω_R and \vec{q}_R have to be consistent with the dispersion relation $\omega(\vec{q})$ of phonon excitation modes. This poses very strict conditions for Raman scattering whereby the change in momentum of a scattered photon and that of energy transferred have to lie on the phonon dispersion curve $\omega(\vec{q})$. Consequently, if a low NA objective is employed, the angle of emission of Raman photons is restricted due to the small range in which \vec{K}_i can vary, limiting the angle of emission of outgoing Raman photons. This explains why we observed such a small enhancement effect for silicon.

Now, let us proceed to the other samples. For the remaining three samples, we observed a much larger enhancement factor. This may not be surprising since all these samples are turbid and the translational symmetry is broken, meaning there is no rigorous relation between ω_R and \vec{q}_R , relaxing the restriction on the momentum \vec{K}_o of outgoing photons. In addition, Raman photons are more likely to be scattered in a turbid sample, increasing the possibility of large-angle emission of Raman photons. Previous studies show that in turbid media, the angular distribution of emissions strongly depends on the reduced scattering coefficient in the turbid media. Fluorescence emission is close to Lambertian for samples with large reduced scattering coefficients [25]. We expect that this argument also holds for Raman scattering, since both are incoherent scattering. For the sample HT, we expect that the reduced scattering coefficient is large, since it is opaque and made of starch powder compressed into a tablet. In R6G, the silver particles can also serve as the scattering centers, increasing the reduced scattering coefficient. For the bacon fat sample, relatively small enhancement effects were observed, suggesting a relatively small scattering coefficient.

To verify the relation between the enhancement factor and turbidity, we need a series of samples with controlled reduced scattering coefficients (turbidity). We chose a mixture of Polydimethylsiloxane (PDMS) gel and TiO₂ microbeads for this purpose. The benefits of this choice are two-fold. Firstly, PDMS has a relatively large Raman scattering cross-section and pure

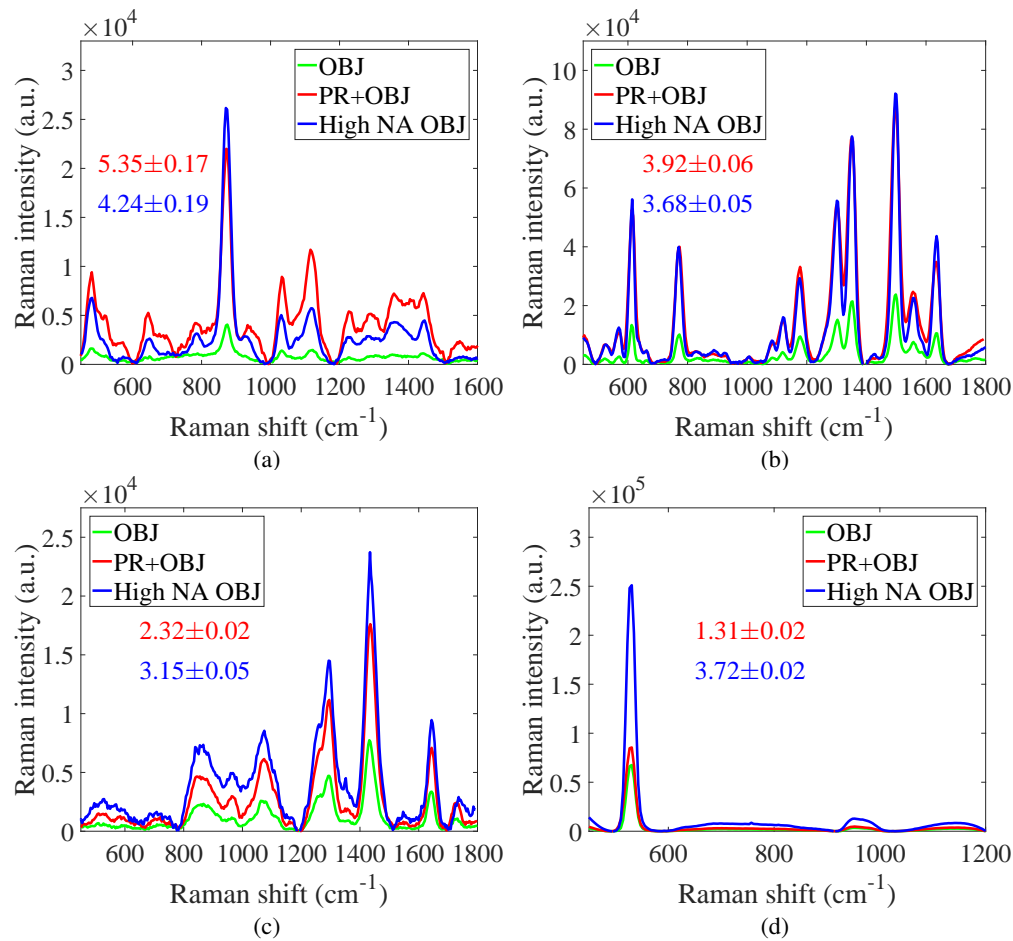


Fig. 2. Raman spectra taken with the PR (red), without the PR (green), and the high-NA objective (blue). The enhancement factors with the standard errors from fits are shown in text in the plot. The red and blue texts are for the spectra taken with the PR and with the high NA objective respectively. (a): a hydrotalcite tablet. (b): Rhodamine 6G dissolved in an agarose gel media. (c): a piece of bacon fat. (d): a piece of crystalline silicon.

PDMS is transparent, meaning that we can observe the enhancement effect on a sample with zero turbidity. Secondly, TiO_2 microbeads are non-absorptive at 632.8 nm and have very weak Raman signals, making it an ideal compound to control the turbidity without affecting the Raman spectra of PDMS. In this study, six Polydimethylsiloxane (PDMS) liquid samples mixed with different volume fractions of TiO_2 microbeads ($d = 1.5 \mu\text{m}$) were prepared. Then, all the samples were stirred and mixed with the PDMS curing agent. After mixing, the liquids were hardened by placing them on a 50°C hotplate for 24 hours. The chosen volume fractions (reduced scattering coefficient) were 0 (0 cm^{-1}), 0.0002 (2.3 cm^{-1}), 0.0006 (5.5 cm^{-1}), 0.0011 (10.3 cm^{-1}), 0.0016 (15.1 cm^{-1}) and 0.0023 (21.3 cm^{-1}) where the reduced scattering coefficients were calculated using the standard Mie scattering theory [26]. The Raman spectra of the pure PDMS are shown in Fig. 3(a). The three fingerprint Raman peaks of PDMS between 400 cm^{-1} to 700 cm^{-1} are clearly visible and they were used to extract the turbidity dependent enhancement factors which are shown in Fig. 3(b). As can be seen from the plot, the enhancement factor increases monotonically from 1.56 to 3.78 as the reduced scattering coefficient rises, validating our hypothesis.

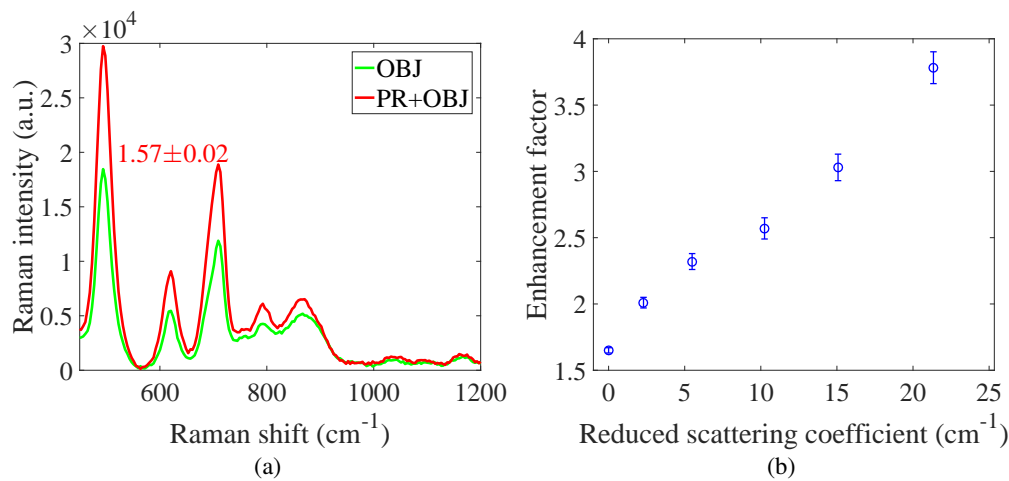


Fig. 3. (a). Raman spectra of pure PDMS. The enhancement factor obtained with Eqn. 1 is shown in text. (b). Turbidity dependence of the enhancement factor for PDMS mixed with TiO_2 microbeads. The turbidity (represented by the reduced scattering coefficient) of the samples was varied by changing the volume fraction of the microbeads.

It is worth noting that Kong *et al.* and Tanaka *et al.* have done similar enhancement studies using non-imaging optics [19, 20]. There, a compound parabolic concentrator was used to collect the Raman signal from an illuminated area. A seven-fold enhancement of BaSO_4 powder and human tissues spectra was achieved compared to the spectra obtained with the 0.29-NA optics. Misra *et al.* also achieved an enhancement of Raman signals using micro-cavity substrates, where a 10x objective was used for signal collection [17]. It can be inferred from Fig. 3 and Fig. 7 of Ref. [17] that a factor of seven times enhancement was obtained in the mustard oil and R6G samples. To compare the performance between their experiments and ours, an NA correction is needed, since the referenced Raman spectra were obtained by collection optics with different NAs. For the results obtained with non-imaging optics the correction ratio is $0.4^2/0.29^2 \approx 1.9$ where 0.4 (0.29) is the NA of our (their) light collection optics. After the correction, the seven-fold enhancement would become a factor of $7/1.9=3.7$ when a 0.4-NA objective lens is used. The comparison between ours and Misra's is less straightforward since the numerical aperture of the collection optics, 10x objective, was not listed in the paper. Therefore, we assign 0.25 to the NA of the 10x objective, which is the most common value for a 10x objective. Following the same procedure, we found a factor of $7/2.56=2.7$ ($0.4^2/0.25^2 \approx 2.56$). Therefore, our results on turbid samples are comparable to theirs.

Now let us consider the possibility of a further increase of the enhancement effect. As mentioned previously, the setup does not make full use of the PR since some portion of the light which would be collected by the PR will be blocked by the barrel of the objective. Thus, if one can use an objective with less beam blockage and replace the 4-inch optics with larger optics (ie. 5-inch optics) to match the diameter of the aperture of the PR, a higher enhancement effect should be achieved. It is worth mentioning that, since we use a long working distance objective (3.9 mm) and the reflector is located at a position far from the sample, the actual working distance is fairly large. In addition, we achieve this without sacrificing the collection efficiency. Thus, this setup can be easily adapted to fit applications where both high collection efficiency and long working distance are necessary.

5. Summary

We have demonstrated a novel way to enhance Raman signal through a parabolic reflector. Our results show that this method is more applicable for turbid samples. A variation of this setup would be very useful in a scenario whereby both long working distance and high collection efficiency are indispensable.

6. Appendix

6.1. Selection of parabolic reflector

To reduce cost, we chose from off-the-shelf parabolic reflectors instead of customizing one. Thus, the right choice of the parabolic reflector would be crucial to achieve the best enhancement effect. Two parameters are particularly important in our decision making namely: the range of angle of acceptance and the outer diameter. A large range of angle of acceptance would result in a high collection efficiency but in the meanwhile increase the outer diameter. The larger the outer diameter, the bigger size of optics it requires to collect all light reflected by a PR. As will be pointed out later, 4-inch or smaller optics are what we found commercially available with a reliable optical quality. Thus, the chosen PR has to be compatible with 4-inch or smaller optics. After searching through the commercially available parabolic reflectors, we found that the one we used in our experiment suited the requirements best (Newport Corporation, PARAB-01, diameter = 101.6mm, $f = 10.2$ mm, clear aperture = 124.5 mm).

6.2. Beam expander design

In order to collect all the Raman photons reflected by the parabolic reflector (PR), the beam size has to be shrunk to be compatible with one inch optics. However, no commercially available beam expander compatible with such a large beam size can be found. We designed one on our own using off-the-shelf lenses to reduce the cost. The diameter of the light beam reflected by the PR is about **90** mm, which means a positive four-inch lens is necessary for the beam convergence. One also needs to choose a beam shrinkage ratio to achieve a tight spot for collection. When the light reaches the collection lens (CL), the beam-size has to be reasonably small otherwise the large spherical aberration would result in a poor focus. However, the design of a beam expander with a large shrinkage ratio is tricky and usually results in a poor optical performance. Therefore, a trade-off was made to achieve a shrinkage ratio of about **eight**. Additionally, we wanted the optical path to be as compact as possible. Bearing these requirements in mind, we started with a simple Galilean beam expander which consists of a plano-convex lens and a plano-concave lens. The

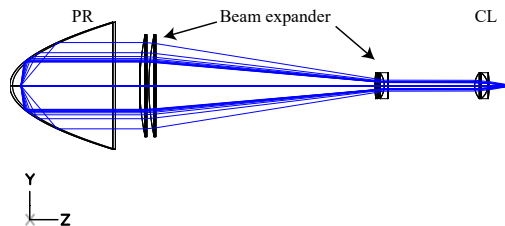


Fig. 4. Schematics of the designed beam expander. Abbreviations refer to the following: collection lens (CL) and parabolic reflector (PR).

benefits of this choice are two-fold. Firstly, the separation between the two lenses is the difference in the their focal lengths, making this configuration compact. Secondly, the positive spherical

aberration induced by the convex lens can be balanced by the negative aberration of the concave lens. After deciding on the type of beam expander, one also needs to determine the focal lengths of the two lenses. After searching through the commercially available lenses, the focal length of the positive (negative) lens was set to be about 250 (-30) mm to start with initially. As is known, the spherical aberration coefficient of a lens grows quartically as the diameter of the lens increases. Given the large size (four inches) of the positive lens, we expect a large spherical aberration coefficient from a simple plano-convex lens. Therefore, we adopt the common trick: replace the positive lens with two identical plano-convex lenses (Comar Optics Ltd. $f = 500\text{mm}$, 500 PQ 100) with double the focal length [27]. To adjust the spherical aberration on the negative lens side, other than the plano-concave lens (Thorlabs, Inc, $f = -30\text{mm}$, LC2679-B), a meniscus lens (Thorlabs, Inc., $f=300\text{m}$, LE1929-B) was placed, making the spherical aberration slightly over corrected to compensate for the positive spherical aberration of the CL. The design, including the PR and the CL, is shown in Fig. 4. We can see that the beam expander is capable of shrinking the beam size and delivering the light to the CL.

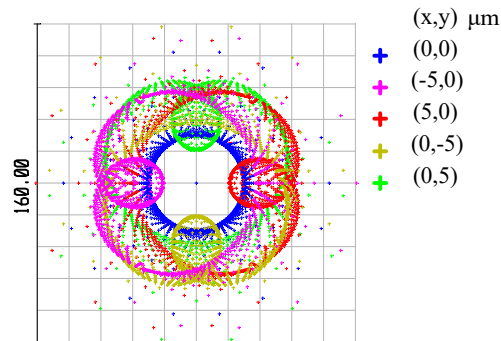


Fig. 5. The spot diagram ray-tracing results at the imaging plane. There are five patterns, the central (blue) one is the spot diagram generated at the focal point of the PR. The other four are the points 5 or -5 μm away from the focal point along the x or y direction.

6.3. Optical performance of the beam expander

We can gain more quantitative insight by looking at the ray-tracing results (shown in Fig. 5). Having experimentally determined that the laser spot size formed by the objective was 10 μm , we can perform a ray-trace of the scattered light to the imaging plane. We show the resultant spot diagram, assuming the focal point of the PR is aligned, together with those formed by light emitted when 5 μm or -5 μm , on either the x or y axis, away from the focal point of the PR. In total, five spot diagrams denoted by different colors are shown. The simulation suggests that the majority of lights are focused within a circular region about 100 μm in diameter.

6.4. Alignment of parabolic reflector

As mentioned in the main text, the alignment between the objective lens and the PR is critical for the optical performance. Ideally, the optical axis of the PR should overlap that of the objective lens. To ensure this, the PR was mounted on a kinematic mount and a tri-axis translation stage which gave us five degrees of freedom (yaw, pitch, x,y and z). However, to adjust so many degrees of freedom at one time is challenging. We came up with a method that simplifies this process by separately adjusting the rotational and translational degrees of freedom. We first started with the rotational degrees of freedom: yaw and pitch. To align the yaw and pitch of the PR with the laser, we removed the objective lens and translated the PR off-center to let the collimated laser beam

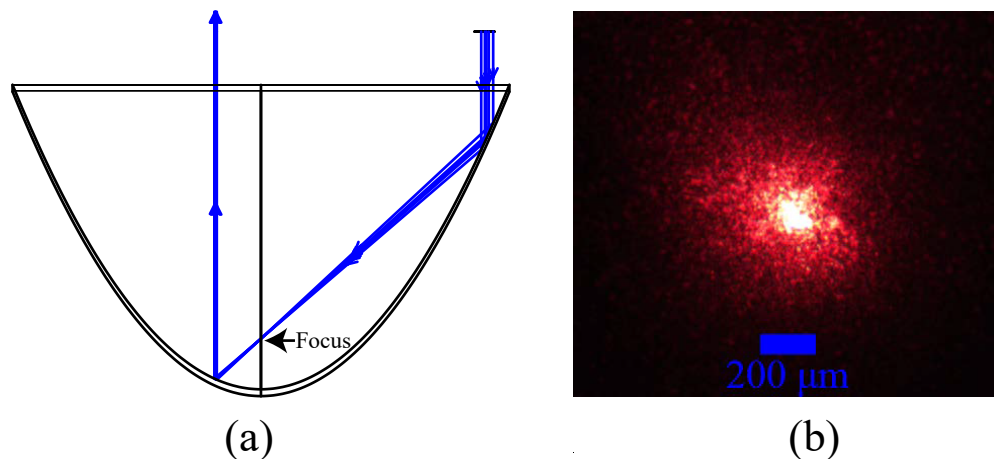


Fig. 6. (a) Schematics of the alignment procedures of PR. If the optical axis is well aligned, the collimated light travelling down would be reflected by the PR towards the focus. After travelling through the focus, the light is reflected again on the opposite side of the PR and collimated upwards. (b) The optical image of the scattered laser light by a piece of paper. The RMS of the spot size was determined to be $150\ \mu\text{m}$, agreeing reasonably well with the ray-tracing results.

hit on the surface near the outer edge of the PR. Then, the beam would be focused towards the focal point of the PR and be reflected upwards. If the optical axis of the PR is parallel to the laser beam, one would expect a collimated beam travelling out of the PR. Moreover, the beam propagating downwards is close to the edge of the PR. Therefore, the resulting size of the beam travelling upwards would be small, making it easier for collimation. We adjusted the yaw and pitch knobs on the kinematic mount to ensure the reflected laser beam was collimated. This step is illustrated in Fig. 6(a). After this step, the objective was put back and finely tuned such that its optical axis overlapped with the laser beam. Up to now, one would expect that the optical axis of the objective lens and that of the PR are well aligned. What is left is to play with the translational degrees of freedom. This can be done by placing a camera at the image plane to monitor the spot formed by the reflected light and adjusting the other three knobs on the tri-axis translation stage to get a tight spot on the camera. Eventually, all five knobs would be finely tuned to achieve the smallest spot. To verify the alignment procedure, we need to measure the spot size formed at the imaging plane. This was achieved by placing a piece of paper at the focal point of the PR, leading to diffusive scattering of the laser beam. The CMOS camera was used to receive the scattered light. The resulting image is shown in Fig. 6(b). From the image, we can see the spot size of the focused light is around $150\ \mu\text{m}$, agreeing reasonably well with the ray-tracing results.

Funding

MINDEF-NTU Joint Applied R&D Cooperation Programme (MINDEF-NTU-JPP/15/02/02); Tier 1 (No. RG38/14 and RG44/15) and Tier 2 grant (No. MOE2015-T2-2-112) funded by the Ministry of Education in Singapore; NTU-AIT-MUV Programme in Advanced Biomedical Imaging (No. NAM/15004); LKC-SCBE collaborative grant (No. CG-01/16) funded by Nanyang Technological University (NTU).

Disclosures

The authors declare that there are no conflicts of interest related to this article.